

Article

Seismic Response of GFRP-RC Interior Beam-to-Column Joints under Cyclic Static Loads

Rui Guo ¹ , Dan Yang ^{1,2}, Bin Jia ^{2,3,*} and Deyun Tang ⁴¹ School of Civil Engineering, Southwest Jiaotong University, Chengdu 610032, China² School of Civil Engineering and Architecture, Southwest University of Science and Technology, Mianyang 621010, China³ Shock and Vibration of Engineering Materials and Structures Key Laboratory of Sichuan Province, Mianyang 621010, China⁴ China Construction First Group the Fifth Construction Co., Ltd., Beijing 100024, China

* Correspondence: jiabin216@126.com

Abstract: A total of nine specimens were constructed and tested under cyclic loads to investigate the differences in seismic behavior between glass fiber-reinforced polymer (GFRP)-reinforced concrete (RC) joints and RC beam-to-column joints. The experimental parameters included stirrup ratios, axial pressure ratios and concrete strength of the beam-to-column joints. The cyclic loading test results showed that the GFRP-RC beam-to-column joints can withstand significantly high lateral deformations without exhibiting brittle failure. Moreover, the RC beam-to-column joint exhibited significantly higher energy dissipation and residual displacement than the GFRP-RC beam-to-column joint by 50% and 60%, respectively. Finally, a shear capacity calculation method for the core zone of this kind of joint was proposed, which agreed well with the experimental results.

Keywords: glass fiber-reinforced polymer; beam-to-column; seismic performance; shear capacity



Citation: Guo, R.; Yang, D.; Jia, B.; Tang, D. Seismic Response of GFRP-RC Interior Beam-to-Column Joints under Cyclic Static Loads. *Buildings* **2022**, *12*, 1987. <https://doi.org/10.3390/buildings12111987>

Academic Editor: André R. Barbosa

Received: 12 October 2022

Accepted: 11 November 2022

Published: 16 November 2022

Publisher's Note: MDPI stays neutral with regard to jurisdictional claims in published maps and institutional affiliations.



Copyright: © 2022 by the authors. Licensee MDPI, Basel, Switzerland. This article is an open access article distributed under the terms and conditions of the Creative Commons Attribution (CC BY) license (<https://creativecommons.org/licenses/by/4.0/>).

1. Introduction

Traditional reinforced concrete (RC) frame structures absorb earthquake energy through structural deformation. However, when the residual displacement of the structures is too large, they are not conducive to earthquake relief and post-disaster reconstruction. Fiber-reinforced polymer (FRP) composites have been used as an alternative to steel reinforcement because of their favorable properties, such as their high strength-to-weight ratio, corrosion resistance, ease and speed of application, and minimal change in geometry. Aksoylu et al. [1] investigated the effect of web openings on pultruded fiber-reinforced polymer (PFRP) under compressive loads, and the results showed that pultruded profiles with carbon fiber-reinforced polymer (CFRP) wrapping are more likely to increase load carrying capacity of the structure; Mandenci and Özkılıç [2] explored the effect of porosity on the free vibration analysis of functionally graded (FG) beams with different boundary conditions using state space approach and Artificial Neural Networks (ANNs) technique, among others. Vedernikov et al. [3] demonstrated for the first time the possibility of applying large cross-sectional profiles to high-speed pultruded suitable structures.

The mechanical properties of FRP composites embedded in concrete have been widely studied, indicating that the bonding of FRP bars to concrete is sufficient and proving the feasibility of using FRP bars in place of steel reinforcement in concrete components. For example, Tavassoli et al. [4] compared the difference in seismic performance between RC columns and GFRP (glass fiber-reinforced polymer) columns. The results showed that the pier columns still had greater stiffness during a large deformation phase. Through a series of pseudo-static loading tests of RC piers with mixed configurations of steel-FRP reinforcement, Ibrahim et al. [5], Sun et al. [6], and Fahmy et al. [7] investigated whether piers with mixed reinforcement had significantly higher post-yield stiffness and

significantly lower residual displacements and whether their energy dissipation capacity was consistent with that of RC piers. Kun et al. [8] conducted single shear tests on FRP-concrete bond joints with different anchorage types and found that different anchoring forms led to three different damage forms: interface delamination, FRP pull-out, and FRP fracture. The elastic-plasticity of the steel reinforcement was the main reason for the reduction in the RC members' post-yield stiffness. To overcome or reduce this shortcoming, recent studies on the seismic performance of FRP-RC frame structures are prevalent. For example, Ghomi et al. [9] and Hasaballa et al. [10] investigated the seismic performance of T-shaped GFRP-RC concrete beam-to-column joints using shear stress, reinforcement form, and concrete compressive strength as test variables, and their results showed that GFRP-RC concrete beam-to-column joints do not suffer from brittle failure and can withstand high transverse deflection. Mady et al. [11] proved that GFRP-RC concrete beam-to-column joints can reach their design capacity under cyclic loading, while their energy dissipation is significantly lower than that of RC concrete frames. Safdar et al. [12] tested three full-scale GFRP-RC T-connections under reversed cyclic loading to investigate the influence of the anchorage type at the end of the longitudinal bars of the beam on the cyclic performance of GFRP-RC T-connections. There are other ways of using FRP materials are applied in reinforcing concrete structures, such as wrapping. Gemi et al. [13] and Özkılıç et al. [14] studied the effect of FRP composite wrapping on the flexure performance of RC-filled GFRP profile hybrid beams. The ultimate load capacity, ductility, stiffness, energy dissipation capacity, and damage modes of the beams were also determined using a combination of tests and simulations.

Above all, existing studies have indicated that using FRP bars instead of steel reinforcement can further improve the strength, deformation capacity, and post-yield stiffness of frame structures. However, to date, no quantitative analysis has been performed on the seismic performance of GFRP-RC concrete frames, and there is a lack of systematic research on the calculation of the bearing capacity of the core area.

Therefore, this paper presents the pseudo-static tests on nine 1/2-scale concrete beam-to-column joints with different stirrup ratios, axial compression load ratio, and concrete strengths. In addition, the effects of different variables on their seismic performance were evaluated based on the test results. Moreover, as the utilization rate of FRP reinforcement is not considered in the existing equations for calculating the bearing capacity of the joints, a new calculation method was established for the shear bearing capacity of GFRP concrete beam-to-column joint cores based on the concept of the effective strain of GFRP bars.

2. Experimental Investigation

2.1. Materials

2.1.1. Concrete

This study used concrete design strength grades C30, C35, and C40, in adherence with the Chinese design specification of concrete structures, meaning that the design compressive strength values are 30 MPa, 35 MPa, and 40 MPa, respectively. The concrete was mixed with ordinary Portland cement (OPC), medium sand with a fineness modulus of 2.48, water, and crushed stone with a maximum size of 10 mm. The mixture proportions are tabulated in Table 1. During the process of casting concrete under continuous casting, three cubic samples (150 mm × 150 mm × 150 mm) were reserved for each strength grade concrete and then cured for 28 days under the same conditions as the corresponding joint specimens. The main mechanical properties of concrete follow standard test methods (GB/T50081-2002) [15], and the measured values of all materials are summarized in Table 2. The mean strengths of grades C30, C35, and C40 cubic specimens were 31.98 MPa, 36.05 MPa, and 40.86 MPa, respectively. Figure 1 shows the compressive test setup photo of the concrete.

Table 1. Mixture proportion of the concrete.

Grade	G_{\max} (mm)	Quantity (kg/m ³)			
		Water	Cement	Fine Aggregate	Coarse Aggregate
C30	10	218.56	383.44	720.86	1177.15
C35		218.75	446.43	642.86	1191.96
C40		218.94	509.17	621.18	1150.71

Note: G_{\max} is the maximum size of gravel.

Table 2. Material properties of concrete.

Grade	Design Strength f_{cd} (MPa)	Compressive Strength f_c (MPa)			
		Measured Values			Mean Value
C30	30	32.04	31.14	32.78	31.98
C35	35	36.56	34.38	37.21	36.05
C40	40	39.02	42.12	38.45	40.86

**Figure 1.** Compressive test for concrete.

2.1.2. Steel Reinforcement and GFRP Bar

Steel bars with a diameter of 6 mm, 8 mm, and 10 mm and GFRP bars with a diameter of 8 mm and 10 mm were used in this study. The GFRP bars, manufactured with glass fiber with a diameter of 36 μm , was impregnated with a suitable resin system to form a rod pattern. Its strength was determined by tensile tests (shown in Figure 2) according to the recommendations of GB/T 228.1-2010 [16]. From the tensile tests, it can be seen that the plastic contribution of steel reinforcement involved both a region of uniform deformation with all parts of the gauge length elongating to the same amount and a nonuniform region with localized deformation or necking. In the case of the GFRP bars, brittle fracture occurred in the elastic region (or after only a very small amount of plastic deformation). Furthermore, the mean values of its mechanical properties, including yield strength, ultimate strength, elongation, and elastic modulus, are summarized in Tables 3 and 4.

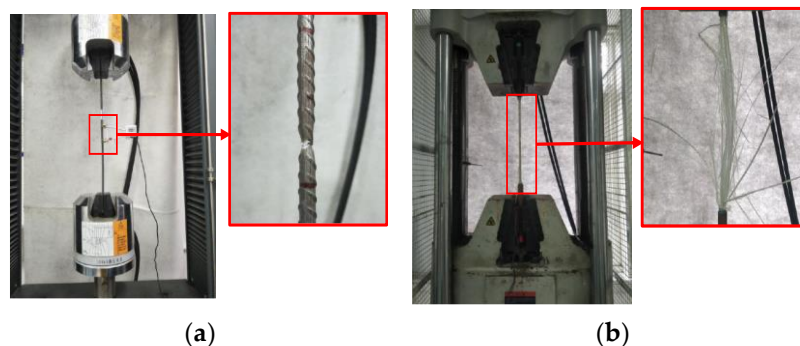
**Figure 2.** Tensile tests for steel and GFRP bars. (a) Steel bars; (b) GFRP bars.

Table 3. Material properties of steel bars.

Diameter (mm)	Yield Strength f_y (MPa)	Ultimate Strength f_{tu} (MPa)	Elongation (%)
6	563.87	647.19	24.03
8	486.61	581.51	22.56
10	480.46	575.16	23.84

Table 4. Material properties of GFRP bars.

Diameter (mm)	Tensile Strength f_{gt} (MPa)	Elastic Modulus (MPa)
6	1481.11	5.67×10^4
8	1317.41	5.35×10^4
10	1153.71	5.03×10^4

2.2. Details of the Specimens

A total of nine joints were fabricated and tested, including eight GFRP concrete beam-to-column joints and one RC concrete beam-to-column joint as a reference specimen, and the scale ratio of all joint specimens was 1/2. The details of the test specimens are shown in Figure 3. The total length of the beam is 3000 mm, the calculated length is 2700 mm, and its cross-section is 175 mm × 250 mm. Meanwhile, to facilitate the lifting and test loading of the joint model, a certain length of loading head is reserved at the top of the column, and the distance from the lateral loading point to the fixed hinge at the base of the column is 1800 mm. The cross-section of the column is 225 mm × 225 mm.

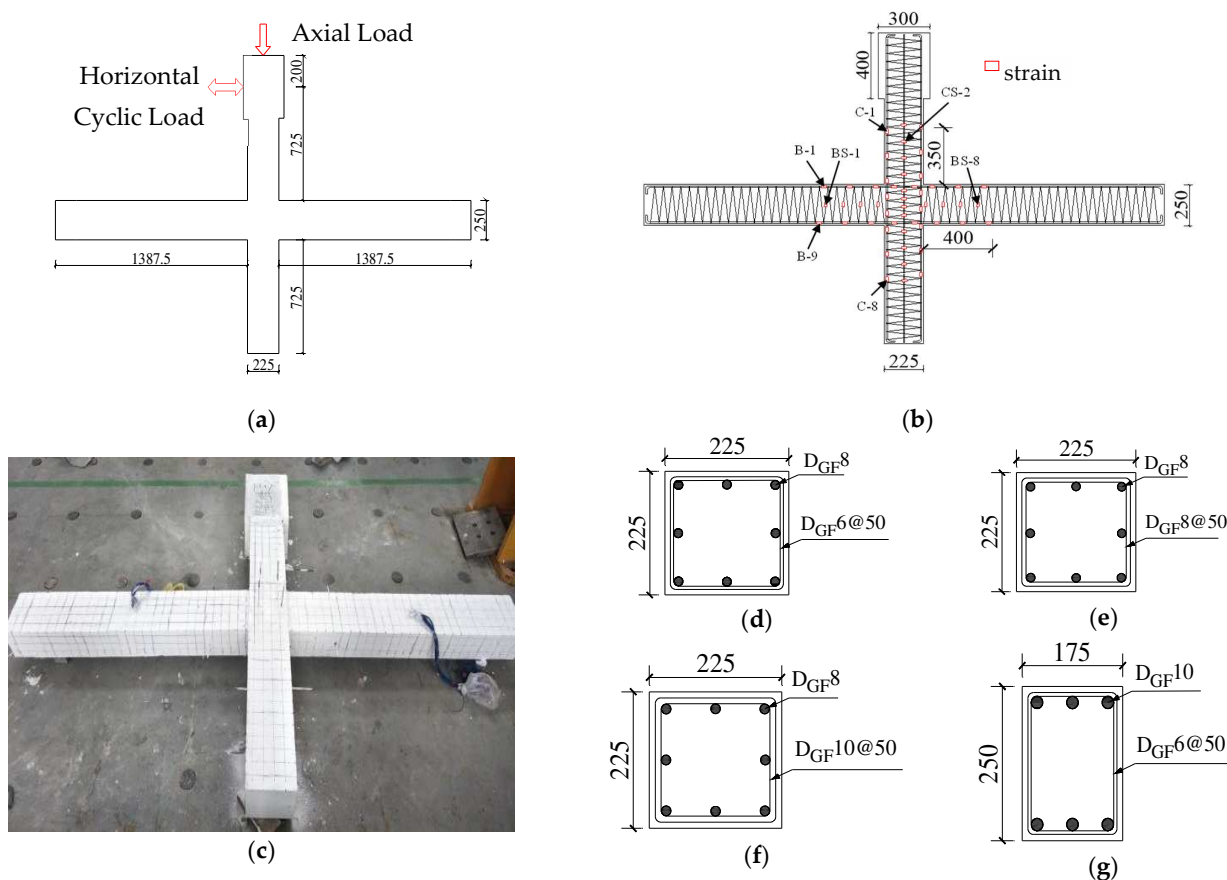


Figure 3. Details of test specimens (units: mm) (a) Dimensions of test specimens; (b) GFRP-RC specimens; (c) Photo of the joints; (d) Column BC-2; (e) Columns BC-5~BC-9; (f) Column BC-4; (g) GFRP-RC Beam.

The test variables in the experiments included the concrete strength, axial compression load ratio, reinforcement type (steel or GFRP bar), and stirrup ratio. Table 5 summarizes the design characteristics of the test specimens, where all joint specimens are made using concrete strengths of grade C40 and steel of HRB400 reinforcement grade. Specimen BC-1 is an RC joint model acting as a control joint with a pouring concrete strength of grade C40 and an axial pressure ratio of 0.1, and the steel stirrup diameter is 6 mm with a spacing of 50 mm. BC-2 to BC-9 are all GFRP concrete beam-to-column joint models, with beam stirrups that are GFRP spiral stirrups with a diameter of 6 mm, wherein BC-2 to BC-4 take the diameter of GFRP spiral stirrups in the column as the variable (6 mm, 8 mm, and 10 mm). BC-5 to BC-7 have different axial pressure ratios (0.2, 0.25, and 0.3) and BC-8 to BC-9 are different with respect to concrete strength (grade C30 and grade C35).

Table 5. Design characteristics of the test specimens.

Specimens	Concrete Strength	Axial Pressure Ratio	Beam		Column	
			Longitudinal Bars	Stirrups	Longitudinal Bars	Stirrups
BC-1	C40	0.1	6 × Φ 10	Φ 6@50	8 × Φ 8	Φ 6@50
BC-2	C40	0.1				D _{GF} 6@50
BC-3	C40	0.1				D _{GF} 8@50
BC-4	C40	0.1				D _{GF} 10@50
BC-5	C40	0.2				D _{GF} 8@50
BC-6	C40	0.25	6 × D _{GF} 10	D _{GF} 6@50	8 × D _{GF} 8	D _{GF} 8@50
BC-7	C40	0.3				D _{GF} 8@50
BC-8	C30	0.1				D _{GF} 8@50
BC-9	C35	0.1				D _{GF} 8@50

Note: Φ means the diameter for HRB400 grade steel reinforcement; D_{GF} means the diameter for GFRP bar.

2.3. Testing Procedure

In this study, a pseudo-static loading test was carried out. As shown in Figure 4, two electrohydraulic actuators were mounted at the top of the column to the reaction frame and reaction wall. The vertical actuator provided a constant axial force and the horizontal actuator applied a cyclic load; the maximum allowable capacity of the horizontal and vertical actuators was 500 and 1000 kN, respectively. Meanwhile, the double hinge devices mounted at the end of the beams were attached to the reaction floor, and the force transducers were arranged on devices to measure the vertical reaction force at the beam end. Moreover, two rods with rolling axes were installed at the top of the column to limit the out-of-plane movement (seen in Figure 4b). To ensure that the rods did not affect the lateral translation of the specimens, it should be noted that one end of the rods was fixed to the vertical reaction frame, and the opposite end had rolling axes supporting the specimen.

Furthermore, the cyclic loads were applied by a displacement-controlled mode until the specimen fractured, which is shown in Figure 5. The cyclic loading procedure consists of several loading steps gradually increasing in lateral displacement, where the displacement increment is 5 mm per step, and three full cycles were conducted for each level. Meanwhile, strain gauges with a diameter of 3 × 5 mm were installed at the plastic hinge zone of the beam and column, respectively, as shown in Figure 3b. A total of 52 strain gauges were used in per specimen. In addition, a total of 14 displacement sensors were used to obtain the average curvatures of column and beam at different displacement levels. The displacement sensors were arranged in the potential plastic hinge zone and core of the beam and column.

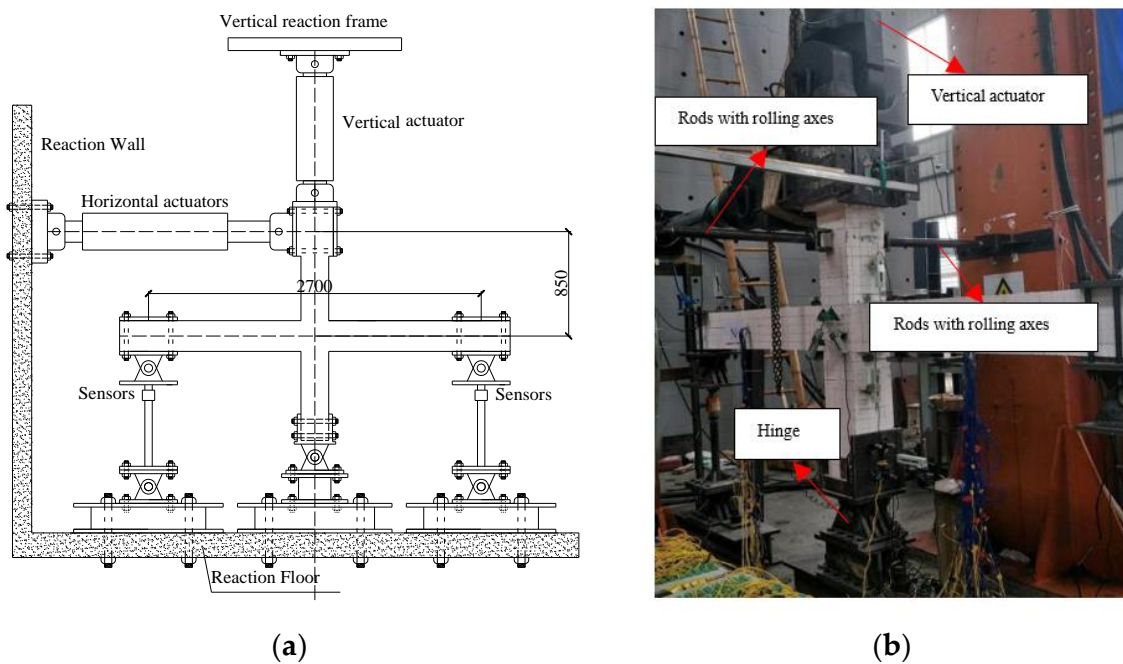


Figure 4. Loading setup. (a) Loading setup; (b) Photo of setup.

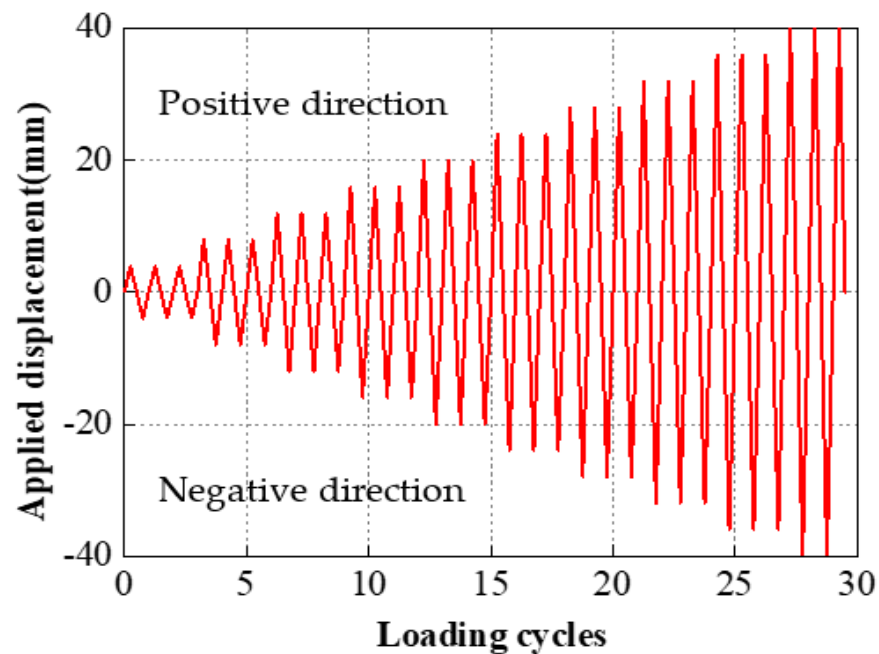


Figure 5. Loading protocol.

3. Test Results and Discussion

3.1. Crack Pattern and Failure Mode

Figure 6 shows the failure mode of each joint specimen after testing. The cracks of all specimens are mainly concentrated in the plastic hinge area of the beam; however, a few cracks occur in the non-core area of the columns, and all joint specimens undergo concrete cracking and cover concrete spalling. During the test, the first vertical bending crack appeared at the beam-to-column junction when the displacement of the column top was ± 4 mm. As the cyclic load increased, a large number of cracks appeared in the plastic hinge area of the beam. Thereafter, when the cyclic load approached the peak load,

cracks appeared in the beam-to-column intersection line and core area, except in the case of specimens BC-5, -6, and -7.

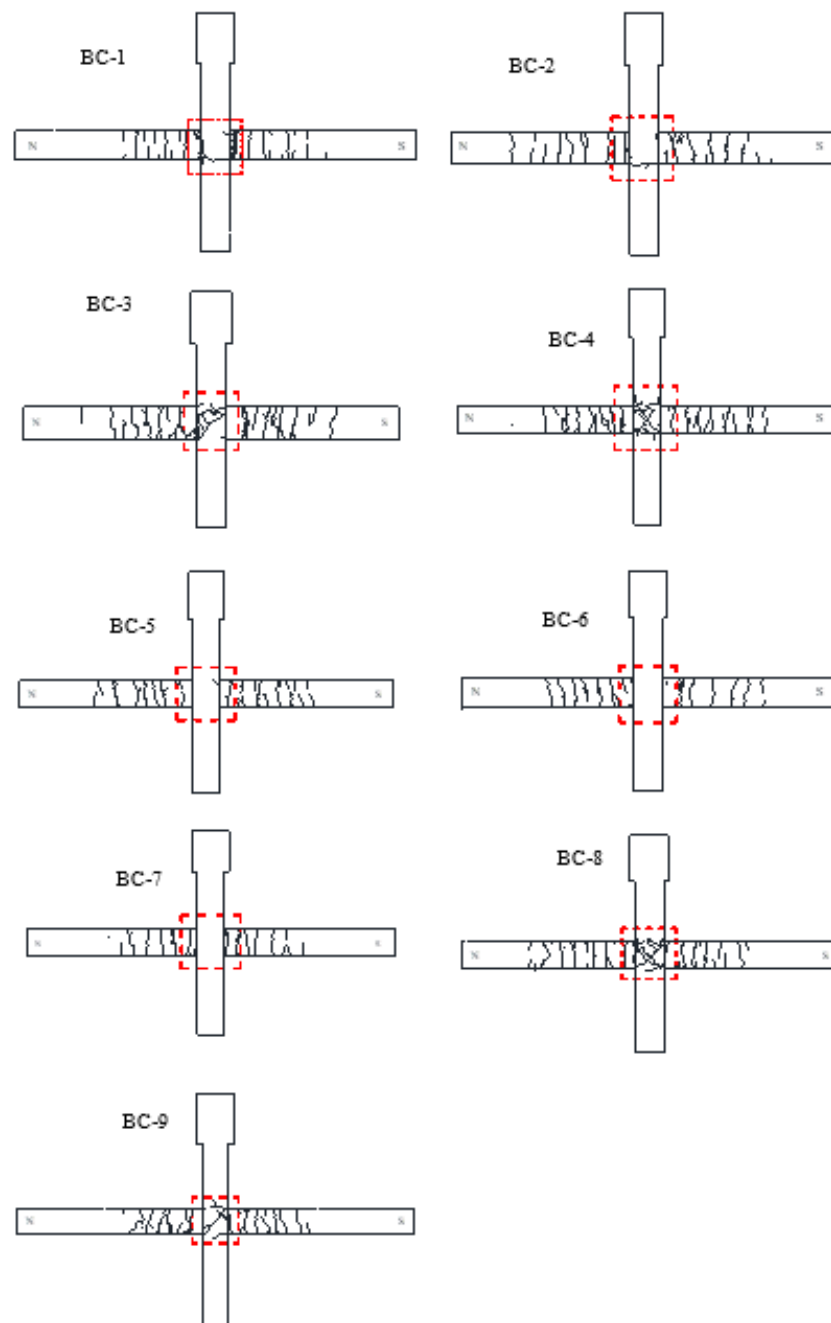


Figure 6. Crack pattern after testing.

Compared to the RC joint specimen (BC-1), the GFRP beam-to-column joints emitted a brittle sound of fiber bundle breakage when the concrete spalled. Therefore, the surface concrete of the beam end where the cracks were concentrated was chiseled away to observe the damage situation of the GFRP, as shown in Figure 7. It can be inferred that the outer rubber layer of the GFRP was pulled off first due to the cyclic load, then the fiber filament bundle gradually appeared to fracture as the load increased, and finally, the internal rubber layer fragmentation occurred in a large area. From the observed damage of the GFRP, it can be concluded that, although GFRP are brittle materials, the GFRP joints still have some energy dissipation capabilities. Meanwhile, brittle damage did not appear when the GFRP joint specimens reached a displacement angle of 5.5%, indicating that the GFRP

beam-to-column joints tested can withstand relatively high lateral deformation without brittle damage.



Figure 7. Observed damage of GFRP. (a) Outer rubber layer failure (BC-9); (b) Fiber bundle breakage (BC-3).

3.2. Hysteretic Load–Displacement Loops

Figure 8 shows the hysteresis load–displacement loops obtained from the cyclic loading tests. In the case of the RC joint specimen (BC-1), the total area under the hysteresis loops increases with cyclic loading after it enters the plastic phase, and a pinching phenomenon occurs at the same time. However, the hysteresis loops of specimens with different stirrup ratios and concrete strengths do not show obvious pinching phenomena. It can be speculated that the deformation of the reinforcement in the RC joint grows rapidly after yielding, and the relative slip of the concrete and reinforcement increases; however, in the case of the GFRP joints, due to the restraining effects provided by the fiber spiral hoop, the relative slip of the GFRP bars is very small after concrete failure. Therein, the maximum displacement of BC-7, which had the largest axial pressure ratio, was the smallest, and the pinching phenomenon was the most obvious among the GFRP joint specimens. In general, the energy dissipation of the GFRP joint specimens is significantly lower than that of the RC joint.

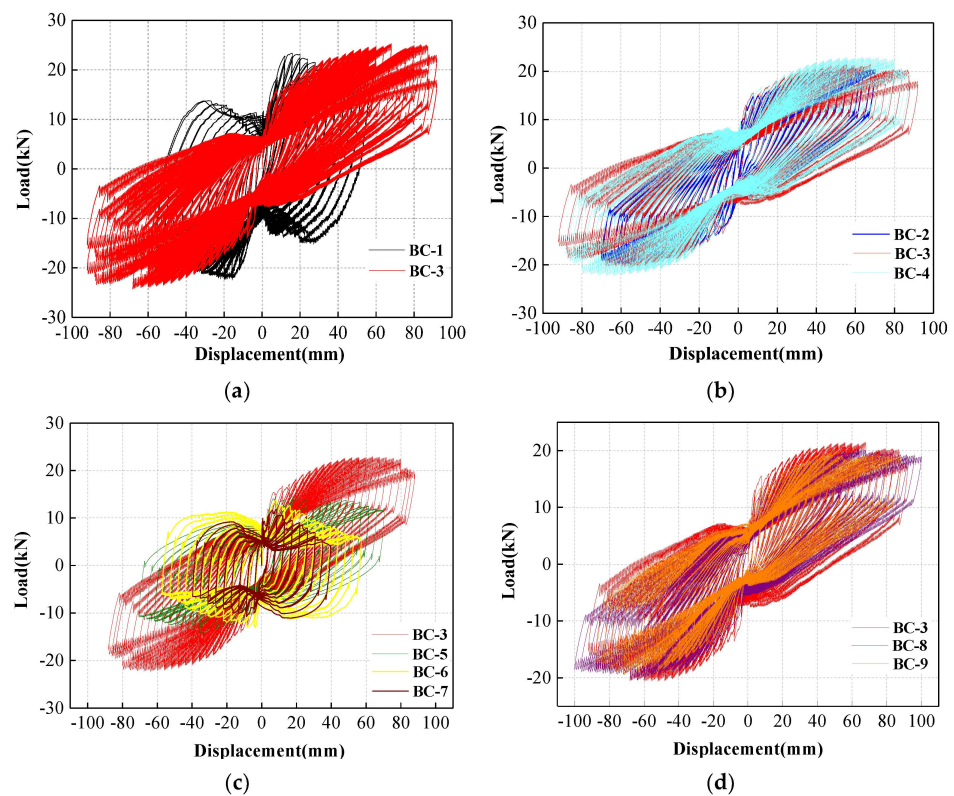


Figure 8. Hysteretic load–displacement loops. (a) RC vs. GFRP; (b) Stirrup ratio group; (c) Axial pressure ratio group; (d) Concrete strength group.

In addition, according to the displacement at the top of the column after test unloading, defined as the residual displacement, the residual displacements in the positive and negative loading directions of the RC joint specimen (BC-1) are basically equal. In contrast, the residual displacements of the GFRP joint specimens have obvious asymmetry and are much smaller, indicating that the GFRP joint has a stronger self-resetting capability than the RC joint.

Figure 9 shows the envelope load–displacement curves of all joint specimens. It seems that the bearing capacity under the same deformation of the RC joint (BC-1) is slightly larger than that of the GFRP joint specimens before the displacement of the column top reaches ± 20 mm because the elastic modulus of the steel reinforcement is much larger than that of the GFRP bars (steel reinforcement: 200 GPa, GFRP bar: 26.7 GPa). However, the gap in bearing capacities among them gradually decreases with horizontal displacement. Compared to the RC joint specimen, whose bearing capacity decreases rapidly after reaching its peak point, the bearing capacities of the GFRP joint specimens decrease slowly, and the curves have obvious plateau sections. Moreover, the bearing capacities of GFRP joints increase with the stirrup ratio; meanwhile, the GFRP joint with a larger axial compression load ratio has a lower peak capacity and poor deformability. The effect of concrete strength on the bearing capacity of fiber-reinforced beam-to-column joints is not significant.

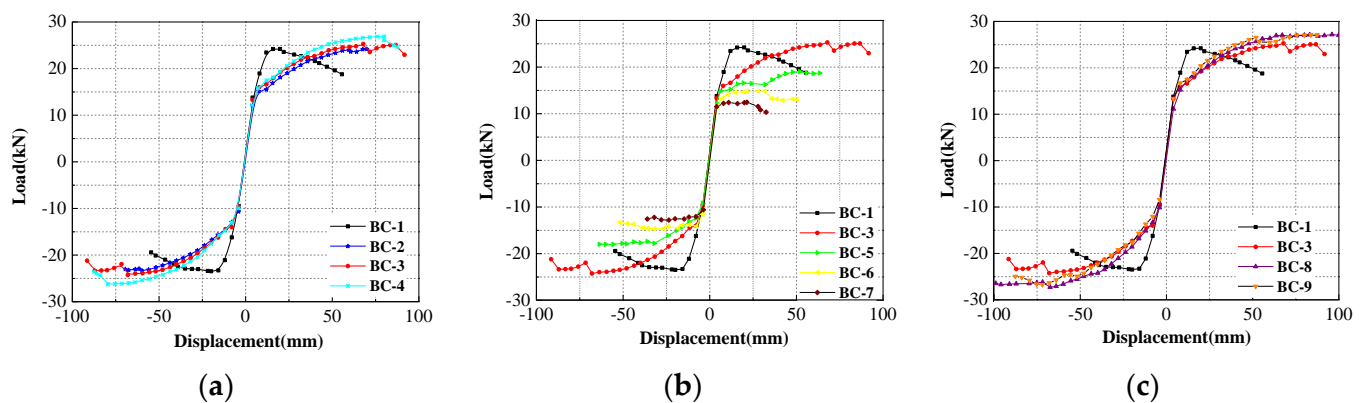


Figure 9. Envelope load–displacement curves. (a) Stirrup ratio group; (b) Axial pressure ratio group; (c) Concrete strength group.

Table 6 summarizes the experimental results of each specimen. The feature points of each specimen are calculated from the skeleton load–displacement curves. The yield point is obtained by graphing the farthest point method proposed by Peng et al. [17], which is the point on the curve farthest from the line connecting the origin and the peak point, and the peak point is the point on the skeleton curve of each joint model with the maximum bearing capacity. It is worth mentioning that the forward yield load of the GFRP joints is lower than that of the RC joints, but deformation exhibits the opposite trend (the deformation of the GFRP joints is significantly larger). Moreover, the yield and peak loads gradually decrease with the axial pressure ratio, and the peak loads of the joints gradually increase with the stirrup ratio. The characteristic values at each point of the beam-to-column section of GFRP bars with different concrete strengths do not significantly differ.

Table 6. Feature points of all joint specimens.

Specimens		D_y /mm	F_y /kN	D_{max} (Drift Ratios)/mm	F_{max} /kN
Positive	BC-1	9.434	20.913	19.884 (2.34%)	24.215
	BC-2	7.664	15.240	69.944 (8.23%)	24.190
	BC-3	7.743	15.975	67.910 (7.99%)	25.288
	BC-4	7.103	15.831	79.998 (9.41%)	26.899

Table 6. Cont.

Specimens	D_y /mm	F_y /kN	D_{max} (Drift Ratios)/mm	F_{max} /kN	
BC-5	6.119	14.775	51.990 (6.12%)	19.020	
BC-6	7.378	13.328	31.754 (3.74%)	14.840	
BC-7	3.992	11.506	21.428 (2.52%)	12.458	
BC-8	11.972	17.326	67.164 (7.90%)	27.024	
BC-9	8.046	16.747	75.584 (8.89%)	27.011	
Negative	BC-1	−12.028	−19.718	−19.882 (2.34%)	−23.475
	BC-2	−8.537	−13.238	−59.806 (7.04%)	−23.339
	BC-3	−7.998	−14.000	−67.988 (8.00%)	−24.268
	BC-4	−10.808	−14.296	−79.500 (9.35%)	−26.279
	BC-5	−7.968	−12.372	−55.702 (6.55%)	−18.011
	BC-6	−3.295	−13.601	−31.940 (3.76%)	−14.668
	BC-7	−3.662	−10.578	−23.606 (2.78%)	−12.794
	BC-8	−19.508	−18.391	−67.472 (7.94%)	−27.265
	BC-9	−19.660	−17.566	−71.938 (8.46%)	−26.735

3.3. Energy Dissipation Capacity

In general, the energy dissipation capacity of the joint member can be calculated by the total area under the hysteresis loops, which is used to express the energy dissipated by the member in the process of an earthquake, as shown in Figure 10. It can be observed that all joint specimens dissipate little energy in their elastic phase; thereafter, the energy dissipation capacities increase since the specimens enter the plastic phase. Therein, the energy dissipation of the RC joint increases abruptly when the displacement of the column top reaches ± 8 mm, which is significantly larger than that of the GFRP joints. However, because large plastic deformation occurs in the RC joint, the damage degree is more serious than that in the GFRP joints; therefore, the energy dissipation capacity increase rate in the RC joint becomes slower, and those of the GFRP joints still grow steadily, indicating that the GFRP joints still have a strong energy dissipation. At the same time, the hysteretic energy dissipation capacity of the GFRP joints is reduced by approximately 50% relative to that of the RC joint. Comparing the GFRP joints, it can be concluded that the energy dissipation capacities increase with the stirrup ratio due to the confinement effect on the concrete by GFRP hoops. Meanwhile, among the axial pressure ratio groups (BC-3, BC-5, BC-6, and BC-7), BC-3, having the smallest axial pressure ratio, consumes the least energy, which implies that an appropriate increase in the axial pressure ratio can lead to an increase in the energy dissipation capacities of the joint members by enhancing the aggregate interlock of concrete. On the other hand, the energy dissipation capacity of specimen BC-8 is lower than those of BC-3 and BC-9. For example, the energy dissipation capacity values of BC-8 is 5.55% and 2.22% lower than that of BC-3 and BC-9, respectively, both being under the +84 mm working condition, indicating that the energy dissipation capacity of the GFRP reinforcement beam-to-column joints increases with increasing concrete strength, but the increase is not obvious.

Furthermore, stiffness degradation is typically used to characterize the stiffness attenuation of joint members under cyclic loading, which can be calculated by the concept of equivalent stiffness, as shown by the following equation:

$$K = \frac{|F^+| + |F^-|}{|\Delta^+| + |\Delta^-|} \quad (1)$$

where F^+ and F^- are the maximum loading values in the positive and negative directions of the hysteresis loops, respectively, and Δ^+ and Δ^- are the displacement values corresponding to the maximum loading in the positive and negative directions of the hysteretic loops, respectively.

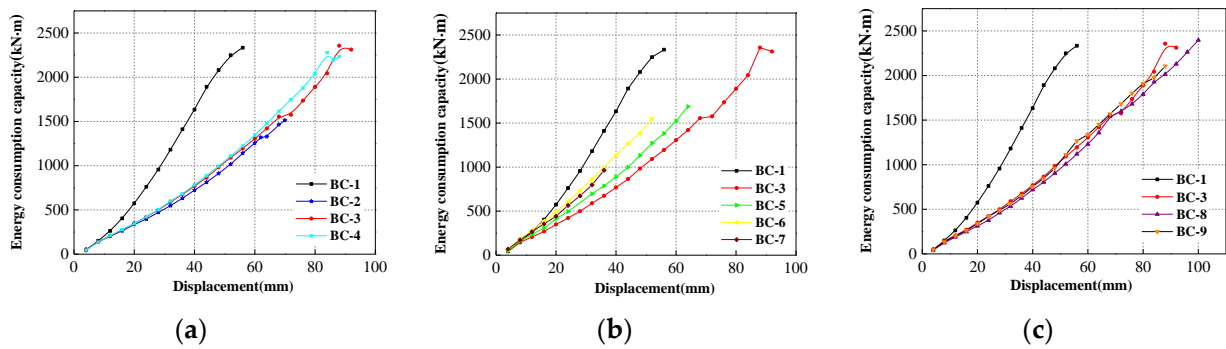


Figure 10. Energy dissipation capacities of joint specimens. (a) Stirrup ratio group; (b) Axial pressure ratio group; (c) Concrete strength group.

Figure 11 shows the stiffness degradation of all specimens during cyclic loading. It appears that the equivalent stiffness of BC-1 is greater than that of the GFRP joints, indicating that the longitudinal reinforcement tension affects its equivalent stiffness after entering the plastic phase due to the smaller elastic modulus of the GFRP bars. Moreover, due to the serious failure that occurred in the plastic hinge region of the BC-1 beam, the rate of stiffness deterioration of specimen BC-1 is faster than that of the GFRP joints. This comparison shows that the stiffness degradation rate of the GFRP joints increases with the axial pressure ratio, with the higher concrete strength specimen having a greater initial stiffness.

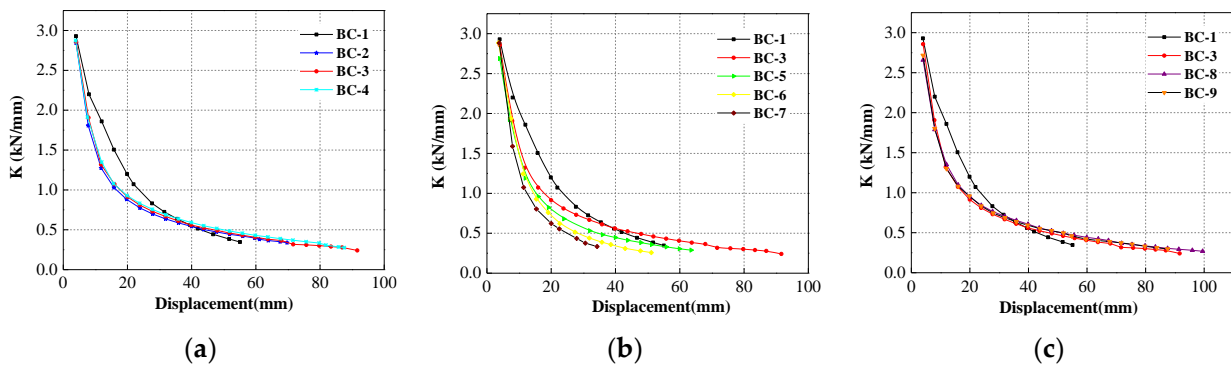


Figure 11. Stiffness degradation of joint specimens. (a) Stirrup ratio group; (b) Axial pressure ratio group; (c) Concrete strength group.

3.4. Stress–Strain Relationship

Strain gauges were arranged along the GFRP longitudinal bars at the end area of the beam in each specimen. Figure 12 shows that the maximum strains observed in the GFRP longitudinal bars are less than half of the rupture strain (approximately 23,000 μ), indicating that the damage of the GFRP bars takes the form of gradual softening without brittle rupture failure. Compared with the RC joint specimen, the strains of the GFRP joint specimens grow slowly without a sudden increase. The strains of the GFRP joint specimens are slightly higher before the steel reinforcement yields; thereafter, the strains of the GFRP joints are significantly lower than those of the RC joint. Furthermore, comparing the GFRP joint specimens with different variables, the GFRP longitudinal bar strain at the same displacement level gradually increases with the stirrup ratio, concrete strength, and axial compression load ratio, and the maximum utilization rate of the GFRP bars can reach 41.8%.

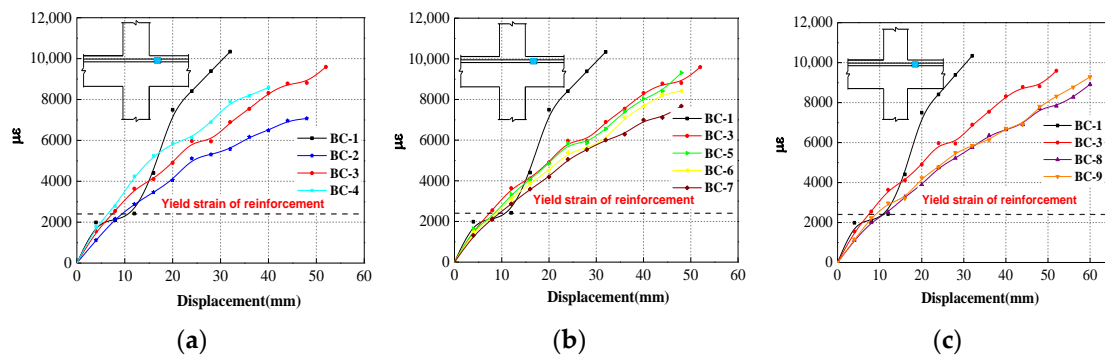


Figure 12. Maximum strains of longitudinal reinforcement. (a) Stirrup ratio group; (b) Axial pressure ratio group; (c) Concrete strength group.

In addition, Figure 13 shows the maximum strains of the GFRP hoops in the core area. As expected, the maximum strain in the RC joint specimen is significantly greater than those in the GFRP joint specimens, indicating that there are greater shear forces occurring in the core area of the RC joint due to the high stiffness of the longitudinal steel beam reinforcement. Comparing the GFRP joints with different variables, the maximum strains of the GFRP hoops increase with the stirrup ratio and decrease with the axial pressure ratio, and the maximum utilization rate captured in the joint stirrups exceeds 11.9% (BC-4). The GFRP hoop strains did not exceed their ultimate strains in the end. In conjunction with the final damage of the specimens, no significant damage occurs in the concrete in the core of the joint specimens, indicating that the reinforcement scheme of GFRP hoops in the core is appropriate for the joint.

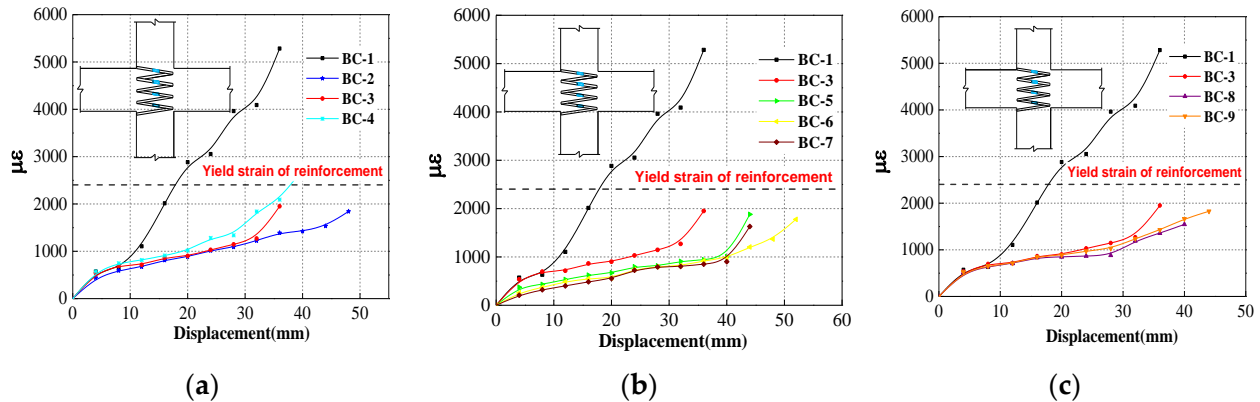


Figure 13. Maximum strains of GFRP hoops. (a) Stirrup ratio group; (b) Axial pressure ratio group; (c) Concrete strength group.

4. Calculation of Load Carrying Capacity

4.1. Nodal Core Shear Bearing Capacity

The reinforced concrete beam-to-column joint is very complex in terms of forces, and the core force transfer mechanism is shown in Figure 14. Its complex hysteretic behavior can be simulated by means of recent accurate and efficient models [18]. In the beam-to-column joint, there are two types of force transmission mechanisms: the inclined compression rod mechanism and the truss mechanism [19]. The diagonal compression bar mechanism (shown in Figure 14b) means that when the joint is subjected to an external load, the concrete pressure C_b at the beam end and the concrete pressure C_c at the column end will cancel a portion of the shear force of the beam-to-column section, forming a diagonal pressure field in the core area of the joint. Figure 14c shows the schematic diagram of the “truss mechanism”. At the beginning of loading, the concrete in the core area bears tensile stress, which gradually increases until it reaches the tensile limit of the concrete. After the

concrete cracks, the hoop reinforcement and vertical longitudinal reinforcement will bear the tensile stress, and the tensile forces T_{bs} and T_{cs} , and pressures C_{bs} and C_{cs} provided by the beam and column reinforcement will offset another part of the beam-to-column section shear force, which will be transferred to the core area to form the shear stress field and act together with the compressive stress field of the diagonal compression bar mechanism to form the truss mechanism [20].

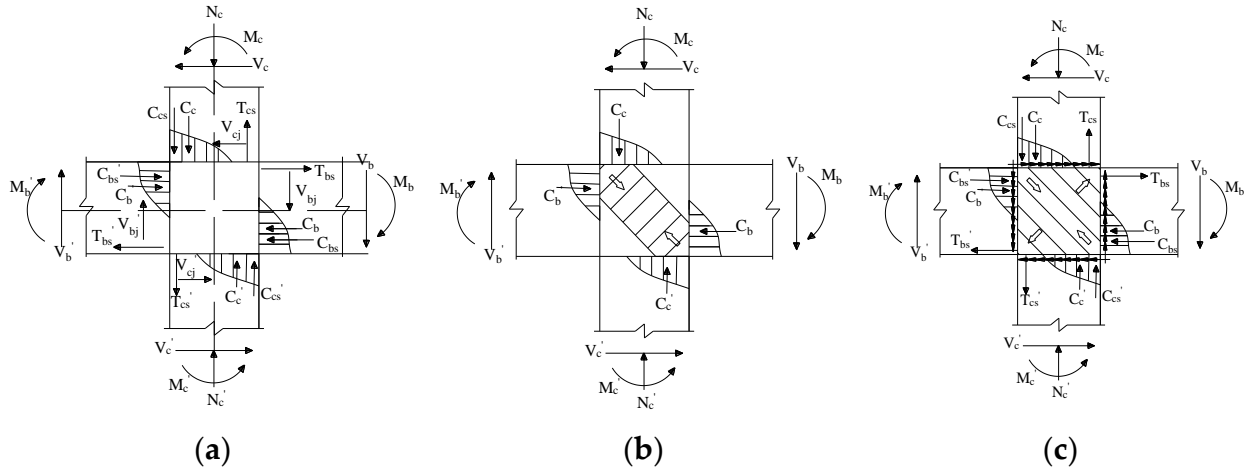


Figure 14. Shear transfer mechanism of joint core region. (a) Nodal force model; (b) Inclined lever mechanism; (c) Truss mechanism.

Referring to the RC concrete beam-to-column joint model and the existing diagonal compression bar model, the shear force is defined as follows [21]:

$$V_j = V_c + V_{SG} \quad (2)$$

where V_c and V_{SG} are the shear forces borne by the concrete and hoop bars, respectively:

$$V_c = \zeta f'_c b_j a_s \cos \theta \quad (3)$$

$$V_{SG} = f_{yv} \frac{A_{SV}}{s} (h_0 - a'_s) \quad (4)$$

The parameters are expressed as follows:

$$\theta = \arctan \left(\frac{h'_b}{h'_c} \right) \quad (5)$$

$$a_s = \sqrt{a_b^2 + a_c^2} \quad (6)$$

$$a_c = \left(0.25 + 0.85 \frac{N}{A_g f'_c} \right) h_c \quad (7)$$

$$\zeta \approx \frac{3.35}{\sqrt{f'_c}} \quad (8)$$

where f'_c is the concrete cylindrical compressive strength; ζ is the concrete compressive strength softening factor; b_j is the effective width of the inclined compression bar [22,23]; a_s is the height of the inclined compression bar; θ is the angle between the inclined compression bar and the horizontal axial direction; h'_b and h'_c are the outermost reinforcements between the beam-to-column cross-section distance; a_b , a_c are the beam-to-column cross-sectional pressure zone heights [24]; c_b is taken as $1/5 h_b$, where h_b is the height of the beam

cross-section; N is the column top axial pressure; A_g is the column gross cross-sectional area; h_c is the column cross-sectional height; f_{yv} is the hoop tensile strength; A_{sv} is the total area of hoop reinforcement configured in the same cross-section; s is the hoop spacing; h_0 is the effective height of the joint cross-section; and a_s' is the distance from the joint point of longitudinal compression reinforcement to the concrete edge of the same cross-section.

In summary, the hoop tensile strength is used to calculate the shear force V_{SG} borne by the hoop reinforcement. According to the proposed static test of the GFRP joint, when the GFRP joints reach their ultimate bearing capacity, the GFRP hoop does not reach its ultimate tensile strain, so the concept of the hoop utilization rate (α) is proposed in this paper. Therefore, based on the influence of the hoop ratio, axial compression load ratio, and concrete strength, the shear bearing capacity of reinforced concrete hoops can be calculated using software to carry out multiple linear regressions on the test data of eight GFRP-reinforced beam-to-column joints. The shear load capacity of GFRP joints is calculated by introducing the hoop utilization rate (α) as follows:

$$V_j = \zeta f_c' b_j a_s \cos \theta + \alpha f_{yv} \frac{A_{sv}}{s} (h_0 - a_s') \quad (9)$$

$$\alpha = 0.0025 f_c - 0.1053 \mu + 2.5501 \rho_{sv} - 0.052 \quad (10)$$

where μ is the axial pressure ratio and ρ_{sv} is the nodal core with the hoop ratio.

4.2. Test Verification

The values of shear bearing capacity obtained from eight GFRP-reinforced concrete beam-to-column joints in this paper are calculated according to Equation (10) and compared with the measured values. Table 7 lists the data of 22 GFRP-reinforced concrete beam-to-column joints in this paper and from other literature.

Table 7. Comparison of shear bearing capacity between theoretical and experimental values.

Specimens	Type	$b_c \times h_c$ /mm	$b_b \times h_b$ /mm	f_c /MPa	f_c' /MPa	μ	$\rho_{sv}/\%$	V_j/kN	V_j'/kN	V_j/V_j'
BC-2	Cross-shaped	225 × 225	175 × 250	43.21	34.57	0.1	0.011	198.677	143.275	1.387
BC-3	Cross-shaped	225 × 225	175 × 250	43.21	34.57	0.1	0.020	202.909	201.938	1.005
BC-4	Cross-shaped	225 × 225	175 × 250	43.21	34.57	0.1	0.031	215.034	176.613	1.218
BC-5	Cross-shaped	225 × 225	175 × 250	43.21	34.57	0.2	0.020	228.932	201.712	1.135
BC-6	Cross-shaped	225 × 225	175 × 250	43.21	34.57	0.25	0.020	242.655	184.479	1.315
BC-7	Cross-shaped	225 × 225	175 × 250	43.21	34.57	0.3	0.020	256.732	180.252	1.424
BC-8	Cross-shaped	225 × 225	175 × 250	32.08	25.66	0.1	0.020	149.640	167.852	0.891
BC-9	Cross-shaped	225 × 225	175 × 250	35.41	28.33	0.1	0.020	165.577	176.671	0.937
G-1.3 [25]	Cross-shaped	350 × 450	350 × 450	38	30.4	0.15	0.024	809.416	968.991	0.835
G-1.8 [25]	Cross-shaped	350 × 450	350 × 450	58	46.4	0.15	0.024	1176.421	976.197	1.205
G-HT-1.0 [9]	T-shaped	400 × 350	350 × 450	47.8	38.24	0.15	0.021	803.343	738.434	1.088
G-HT-1.1 [9]	T-shaped	400 × 350	350 × 450	42.2	33.76	0.15	0.021	708.375	846.611	0.837
J30-0.70 [10]	T-shaped	400 × 350	350 × 450	37.9	30.32	0.15	0.021	635.454	572.949	1.109
J30-0.85 [10]	T-shaped	400 × 350	350 × 450	32.6	26.08	0.15	0.021	545.574	490.602	1.112
J30-1.0 [10]	T-shaped	400 × 350	350 × 450	35.6	28.48	0.15	0.021	596.450	700.334	0.852
J60-0.70 [10]	T-shaped	400 × 350	350 × 450	51.3	41.04	0.15	0.021	867.281	624.406	1.389
J60-0.85 [10]	T-shaped	400 × 350	350 × 450	52.6	42.08	0.15	0.021	879.003	735.861	1.195
J60-1.0 [10]	T-shaped	400 × 350	350 × 450	52.6	42.08	0.15	0.021	879.003	881.301	0.997
H-S [26]	T-shaped	400 × 350	350 × 450	41	32.8	0.15	0.012	671.735	509.039	1.320
H-D [26]	T-shaped	400 × 350	350 × 450	31	24.8	0.15	0.012	503.956	395.719	1.274
B-S [26]	T-shaped	400 × 350	350 × 450	37	29.6	0.15	0.012	604.549	744.982	0.811
B-D [26]	T-shaped	400 × 350	350 × 450	40	32	0.15	0.012	654.871	610.418	1.073
										Mean
										Standard deviation
										Coefficient of variation

The formula for calculating the actual test value is as follows:

$$V_j' = T_l + T_r - V_c \quad (11)$$

where V_j' is the measured shear force; T_l and T_r are the joint left and right beam end tensile steel tensions; and V_c is the column end shear force. The mean value of the ratio between the calculated and measured values of 22 GFRP-reinforced concrete beam-to-column joints is 1.109, the standard deviation is 0.191, and the coefficient of variation is 0.172.

5. Conclusions

To improve the post-earthquake restorability of the RC frame structures, an alternative solution was proposed that uses GFRP bars instead of steel bars in beam-to-column joints. The cyclic response of GFRP was experimentally investigated and the shear capacity of this joints was proposed. The following conclusions can be drawn based on the experimental and numerical results:

1. Under the cyclic displacement load, the damage of the GFRP-RC interior beam-to-column joints is mainly concentrated in the plastic hinge zone at the end of the beam, which is in line with the design concept of a “strong column and weak beam”. At a 5.5% displacement drift ratio, the GFRP-RC interior beam-to-column joints did not show brittle damage, indicating that the joints can withstand significantly large lateral drift ratios.
2. Compared to RC beam-to-column joints, GFRP-RC interior beam-to-column joints have a slow increase in load capacity with increasing drift, while it can reach its design capacity. The use of GFRP bars instead of steel bars in concrete beam-to-column joints can significantly reduce the residual displacement of beam-to-column joints, but their energy dissipation capacity is also reduced.
3. The energy dissipation capacity of the GFRP-RC joints increases with increasing the axial load ratio. However, a large axial load ration can lead to large residual displacement. Thus, a lower axial load ratio is recommended to improve the self-centering capacity of the GFRP-reinforced concrete frames.
4. It is advisable to reduce the axial pressure ratio (less than 0.3) of GFRP-RC interior beam-to-column joints to improve the post-earthquake functionality of GFRP-reinforced concrete frames.
5. A shear capacity calculation method for the core zone of GFRP-RC beam-to-column joints was proposed, which agreed well with the experimental results.

The GFRP beam-to-column joints have high self-centering capacity and weak energy dissipation capacity. Therefore, this manuscript suggests that a certain amount of reinforcement can be allocated in the core area to increase the energy dissipation capacity. In addition, the GFRP and steel bars can be used simultaneously to improve the seismic performance of beam-to-column joints. More studies are needed for the response of the joints under dynamic loads, and the response of the joints need to be simulated by means of hysteretic models [27,28].

Author Contributions: Conceptualization, R.G., D.Y., B.J., and D.T.; Data Curation, D.Y.; Writing—Original Draft Preparation, D.Y.; Writing—Review and Editing, R.G. All authors have read and agreed to the published version of the manuscript.

Funding: This research was funded by the Open Fund Project of Shock and Vibration of Engineering Materials and Structures Key Laboratory of Sichuan Province grant number [No.20kfgk05]. Funder: Shock and Vibration of Engineering Materials and Structures Key Laboratory of Sichuan Province grant number.

Institutional Review Board Statement: The study did not require ethical approval.

Informed Consent Statement: The study did not involve humans.

Data Availability Statement: Some or all data and models generated or used during the study are available from the corresponding author by request.

Conflicts of Interest: The authors declare no conflict of interest.

References

1. Aksoylu, C.; Özkılıç, Y.O.; Madenci, E. Compressive Behavior of Pultruded GFRP Boxes with Concentric Openings Strengthened by Different Composite Wrappings. *Polymers* **2022**, *14*, 4095. [[CrossRef](#)] [[PubMed](#)]
2. Madenci, E.; Özkılıç, Y.O. Free vibration analysis of open-cell FG porous beams: Analytical, numerical and ANN approaches. *Steel Compos. Struct.* **2021**, *40*, 157–173.
3. Vedernikov, A.; Gemi, L.; Madenci, E. Effects of high pulling speeds on mechanical properties and morphology of pultruded GFRP composite flat laminates. *Compos. Struct.* **2022**, *301*, 116216. [[CrossRef](#)]
4. Tavassoli, A.; Liu, J.; Sheikh, S. Glass fiber-reinforced polymer-reinforced circular columns under simulated seismic loads. *ACI Struct. J.* **2015**, *112*, 103–114. [[CrossRef](#)]
5. Ibrahim, A.I.; Wu, G.; Sun, Z. Experimental study of cyclic behavior of concrete bridge columns reinforced by steel basalt-fiber composite bars and hybrid stirrups. *J. Compos. Constr.* **2017**, *21*, 4016091. [[CrossRef](#)]
6. Sun, Z.; Wu, G.; Wu, Z.; Zhang, M. Seismic behavior of concrete columns reinforced by steel-FRP composite bars. *J. Compos. Constr.* **2011**, *15*, 696–706. [[CrossRef](#)]
7. Fahmy, M.F.; Wu, Z.; Wu, G.; Sun, Z. Post-yield stiffnesses and residual deformations of RC bridge columns reinforced with ordinary rebars and steel fiber composite bars. *Eng. Struct.* **2010**, *32*, 2969–2983. [[CrossRef](#)]
8. Kun, D.; Zhipeng, J.; Song, Y.; Derun, D.; Yang, L. Experimental study on bearing capacity of FRP-concrete bonding interface with mechanical end anchorage. *J. Build. Struct.* **2020**, *41* (Suppl. 1), 399–405. (In Chinese)
9. Ghomi, S.; El-Salakawy, E. Seismic performance of GFRP-RC exterior beam-column joints with lateral beams. *J. Compos. Constr.* **2016**, *20*, 04015019. [[CrossRef](#)]
10. Hasaballa, M.H.; El-Salakawy, E. Shear capacity of Type-2 exterior beam-column joints reinforced with GFRP bars and stirrups. *J. Compos. Constr.* **2016**, *20*, 04015047. [[CrossRef](#)]
11. Mady, M.; El-Ragaby, A.; El-Salakawy, E. Seismic behavior of beam-column joints reinforced with GFRP bars and stirrups. *J. Compos. Constr.* **2011**, *15*, 875–886. [[CrossRef](#)]
12. Safdar, M.; Sheikh, M.N.; Hadi, M.N. Cyclic Performance of GFRP-RC T-Connections with Different Anchorage and Connection Details. *J. Compos. Constr.* **2022**, *26*, 04022022. [[CrossRef](#)]
13. Gemi, L.; Madenci, E.; Özkılıç, Y.O. Effect of Fiber Wrapping on Bending Behavior of Reinforced Concrete Filled Pultruded GFRP Composite Hybrid Beams. *Polymers* **2022**, *14*, 3740. [[CrossRef](#)] [[PubMed](#)]
14. Özkılıç, Y.O.; Aksoylu, C.; Yazman, Ş. Behavior of CFRP-strengthened RC beams with circular web openings in shear zones: Numerical study. *Structures* **2022**, *41*, 1369–1389. [[CrossRef](#)]
15. *GB/T50081-2019*; Standard for Test Methods of Concrete Physical and Mechanical Properties. China Architecture & Building Press: Beijing, China, 2019. (In Chinese)
16. *GB/T228.1-2021*; Metallic Materials-Tensile Testing-Part 1: Method of Test at Room Temperature. China Architecture & Building Press: Beijing, China, 2021. (In Chinese)
17. Peng, F.; Hanlin, Q.; Lieping, Y. Discussion and definition on yield points of materials, members and structures. *Eng. Mech.* **2017**, *34*, 36–46. (In Chinese)
18. Vaiana, N.; Sessa, S.; Marmo, F. A class of uniaxial phenomenological models for simulating hysteretic phenomena in rate-independent mechanical systems and materials. *Nonlinear Dyn.* **2018**, *93*, 1647–1669. [[CrossRef](#)]
19. Tasligedik, A.S. Shear Capacity N-M Interaction Envelope for RC Beam-Column Joints with Transverse Reinforcement: A Concept Derived from Strength Hierarchy. *J. Earthq. Eng.* **2020**, *26*, 1–31. [[CrossRef](#)]
20. Paulay, T.; Park, R.; Priestley, M.J.N. Reinforced concrete beam-column joints under seismic actions. *ACI Struct. J.* **1978**, *75*, 585–593.
21. Danying, G.; Ke, S.; Shunbo, Z. Calculation method for bearing capacity of steel fiber reinforced high-strength concrete beam-column joints. *J. Build. Struct.* **2014**, *35*, 71–79. (In Chinese)
22. Hwang, S.J.; Lee, H.J. Analytical model for predicting shear strengths of interior reinforced concrete beam-column joints for seismic resistance. *ACI Struct. J.* **2000**, *97*, 35–44.
23. Hwang, S.J.; Lee, H.J. Analytical model for predicting shear strengths of exterior reinforced concrete beam-column joints for seismic resistance. *ACI Struct. J.* **1999**, *96*, 846–857.
24. Paulay, T.; Priestley, M.N.J. *Seismic Design of Reinforced Concrete and Masonry Buildings*; John Wiley & Sons: New York, NY, USA, 1992; pp. 210–239.
25. Ghomi, S.K.; El-Salakawy, E. Effect of joint shear stress on seismic behaviour of interior GFRP-RC beam-column joints. *Eng. Struct.* **2019**, *191*, 583–597. [[CrossRef](#)]
26. Hasaballa, M.H.; El-Salakawy, E. Anchorage Performance of GFRP Headed and Bent Bars in Beam-Column Joints Subjected to Seismic Loading. *J. Compos. Constr.* **2018**, *22*, 04018060. [[CrossRef](#)]

-
27. Vaiana, N.; Sessa, S.; Rosati, L. A generalized class of uniaxial rate-independent models for simulating asymmetric mechanical hysteresis phenomena. *Mech. Syst. Signal Process.* **2021**, *146*, 106984. [[CrossRef](#)]
 28. Yi-Kwei, W. Method for Random Vibration of Hysteretic Systems. *J. Eng. Mech. Div.* **1976**, *102*, 249–263.